

Received February 28, 2019, accepted April 18, 2019, date of publication May 27, 2019, date of current version September 12, 2019.

Digital Object Identifier 10.1109/ACCESS.2019.2919377

Dual-Polarized Spatial–Temporal Propagation Measurement and Modeling in UMa O2I Scenario at 3.5 GHz

RUONAN ZHANG¹, (Member, IEEE), **HAOCHEN XU**¹,
XIAOJIANG DU², (Senior Member, IEEE), **DEYUN ZHOU**¹,
AND MOHSEN GUIZANI³, (Fellow, IEEE)

¹Department of Communication Engineering, Northwestern Polytechnical University, Xi'an 710072, China

²Department of Computer and Information Sciences, Temple University, Philadelphia, PA 19122, USA

³Department of Computer Science and Engineering, Qatar University, Doha 2713, Qatar

Corresponding author: Xiaojiang Du (dxj@ieee.org)

This work was supported in part by the National Natural Science Foundation of China under Grant 61571370, Grant 61601365, and Grant 61801388, in part by the Key Research Program and Industrial Innovation Chain Project of Shaanxi Province under Grant 2019ZDLGY07-10, Grant 2019JQ-253, and Grant 2019JM-345, and in part by the China Postdoctoral Science Foundation under Grant BX20180262, Grant BX20190287, Grant 2018M641020, and Grant 2018M641019.

ABSTRACT Outdoor-to-indoor (O2I) coverage in urban areas by using the sub-6 GHz (sub-6G) band is important in the fifth generation (5G) mobile communication system. The spatial-temporal propagation characteristics in different polarizations in the 5G spectrum are crucial for the network coverage. In this paper, we measured the urban macrocell (UMa) O2I channels at 3.5 GHz in the space, time, and polarization domains simultaneously. The channel sounder utilized two $\pm 45^\circ$ polarized antenna arrays. The transmitter (TX) was placed on the rooftop of a five-storey building to emulate a base station and the receiver (RX) was moved in the corridors on different floors in another building to emulate user equipments (UEs). We obtained the small-scale parameters of excess delay, power, and azimuth/elevation of arrival (AoA/EoA) of individual multipath components (MPCs), the propagation profiles of azimuth/elevation power spectrum (APS/EPS) and power delay profile (PDP), and the large-scale parameters including azimuth/elevation spread of arrival (ASA/ESA) and delay spread (DS). Based on the measurement results, we propose the lifted-superposed Laplace distribution (LS-Laplace) function and lifted-superposed normal distribution (LS-Normal) function to model the APS and EPS, respectively, and a three-phase model for the PDP. We find that the ASA and ESA follow the lognormal distribution and the DS has a Rayleigh distribution. We also reveal the impact of surrounding environments and polarization on the channel propagation profiles and statistical characteristics. The measurement results and channel models in this paper provide reference for the design and deployment of the 5G system to exploit the spatial and polarization diversities in the UMa O2I scenario.

INDEX TERMS Propagation measurement, channel modeling, 5G, dual-polarization, outdoor-to-indoor, power spectrum.

I. INTRODUCTION

In the deployment of cellular networks, the outdoor-to-indoor (O2I) coverage in urban areas is an important scenario for service provisioning. In the fifth generation (5G) mobile communication system, the active antenna units (AAUs) of next generation NodeBs (gNBs) installed on building rooftops or towers can provide O2I coverage in macrocells by using the sub-6 GHz (sub-6G) spectrum, especially in the standalone (SA) 5G-NR (new radio).

The associate editor coordinating the review of this article and approving it for publication was Kostas Psannis.

Massive multiple-input-multiple-output (MIMO) is a key technology in 5G and expected to be adopted on AAUs [1], [2]. Massive MIMO performs full-dimensional and high-granularity beamforming and thus provides significant system capacity gain by exploiting spatial multiplexing. The performance of beamforming depends critically on the spatial propagation characteristics of the radio channels, such as the angular power spectrum and angular spread. In addition, AAUs will employ dual-polarized antenna elements to further improve the spectrum efficiency by polarization diversity. The correlation between the channels with cross polarizations determines the polarization

diversity gain. Therefore, the radio propagation characteristics in 3-dimensional (3D) space with different polarizations are critical for the signal strength and coverage range using the 5G technologies. We need to study the propagation characteristics in the time, space, and polarization domains simultaneously and establish accurate channel models for the sub-6G frequency band [3]. To the best of our knowledge, the channel propagation has not been fully investigated for the candidate 5G spectrum in the O2I scenario and is still an open issue to address.

In this paper, we present a measurement campaign in the urban macrocell (UMa) O2I scenario. In the 5G standardization, 3.5 GHz has been selected as a commercial frequency in the sub-6G band for macrocell coverage. The purpose of our campaign is to obtain the spatial and temporal multipath component (MPC) parameters and the radio propagation profiles in cross polarizations, and establish accurate spatial-temporal statistic channel models. In addition, we analyze the effect of scattering environments and polarization on the radio propagation characteristics. The main contributions of this paper are two-fold.

First, we measured the 3D radio propagation utilizing a multi-domain channel sounder in a typical UMa O2I scenario. Both the transmitter (TX) and receiver (RX) used a $\pm 45^\circ$ polarized antenna array. The TX (emulating a gNB) was installed on the rooftop of a 5-storey building and the RX (emulating a user equipment, UE) was moved on the 1st, 2nd, and 3rd floors in another building about 200 meters away. We measured the channel propagation parameters and profiles in the cross polarizations, including:

- 1) the small-scale MPC parameters including excess delay, azimuth/elevation angle of arrival (AoA/EoA), and power of each individual propagation path,
- 2) the large-scale channel parameters including root-mean-square (RMS) delay spread (DS) and RMS azimuth/elevation spread of arrival (ASA/ESA), and
- 3) the propagation profiles including power delay profile (PDP) and azimuth/elevation power spectrum (APS/EPS).

Second, we propose a series of stochastic models for the propagation profiles and parameters based on the measurement results as follows.

- 1) We propose a lifted-superposed Laplace distribution (LS-Laplace) model and lifted-superposed normal distribution (LS-Normal) model for the APS and EPS, respectively. The distribution of the parameters in these models are obtained by fitting the functions to the measured angular power spectra. The proposed models not only describe the clustering behavior in the power arrival over the incident angles but also incorporate the power floor contributed by the scattered MPCs that arrive at the RX quite uniformly.
- 2) In the time domain, we propose a three-phase model for PDP that includes the rising, dropping, and trailing stages. The measurement results show that the

MPC clusters overlap in the time domain and the model can describe the pattern of the variation of the power arrival with respect to excess delay.

- 3) For the large-scale channel parameters, we propose to model ASA and ESA by the lognormal distribution and DS by the Rayleigh distribution. The distribution parameters are determined based on the calculated values from the measured power spectra.
- 4) We also analyze the impact of polarization by evaluating the correlation between the APSs, EPSs, and PDPs in $\pm 45^\circ$ polarizations. The results show that polarization does not introduce significant effect on the multipath propagation profiles in both the space and time domains.

The measurement results and proposed models reveal the multipath propagation characteristics in the space, time, and polarization domains. This work can be used for the design and performance evaluation of the 5G technologies and network coverage optimization in the UMa O2I scenario using the sub-6G band [4].

The rest of the paper is organized as follows. Section II overviews the previous measurement campaigns on the spatial-temporal channels in cellular network scenarios. Section III presents the multipath spatial-temporal channel model and the key channel parameters. Section IV introduces the measurement scenario and channel sounder in our campaign. The measurement results and models for the spatial propagation characteristics including APS, EPS, ASA, and ESA are presented in Section V. The temporal propagation characteristics including PDP and DS measurement results and models are presented in Section VI. Section VII analyzes the impact of polarization by evaluating the correlation between the cross-polarized channels. Section VIII concludes the paper and points out future study issues.

II. RELATED WORK

To establish accurate 3D channel models for cellular networks, a large amount of effort has been made to develop channel sounders and measure the radio propagation in practical environments [5]. To support the statistical channel modeling in urban environments, the authors in [6] carried out a 3D MIMO channel measurement campaign in the UMa and UMi (urban microcell) O2I scenarios in the 2.52 to 2.54 GHz band. The results suggested that the ESA reduced with the decreasing of the BS height and there was no clear pattern for the ASA. The authors in [7] utilized the ray-tracing method to evaluate the EPS in the urban O2I scenario. It was found that the EPS at low-rise floors fitted the Laplace distribution well, while the EPS at the high-rise floors fitted the double-Gaussian functions. The authors in [8] performed measurement at 3, 10, 17, and 60 GHz in the O2I scenario and found that the power attenuation was relatively low and frequency-independent for the non-coated glass windows and was high and increasing with frequency for the coated glass windows. In [9], through a measurement campaign in the UMa I2O scenario at 2.6 GHz, the authors found that

the probability distribution function (PDF) parameters of ESA were independent to the UE height and position in the non-line of sight (NLOS) case. The authors in [10] measured the vehicle-to-vehicle channels at 5.3 GHz with a bandwidth of 60 MHz in suburban, urban, and underground parking lot environments. The results suggested that the MPC lifetime could be fitted by a linear polynomial function and the small-scale fading had the Nakagami distribution.

The authors in [11] performed an O2I channel measurement at 3.5 GHz and inspected the MPC clustering behavior. The results suggested that the number of paths in one cluster and the number of clusters fitted the lognormal and normal distributions, respectively. For the quasi-static channels, the authors in [12] conducted a measurement campaign at the frequencies of 11, 16, 28, and 38 GHz in a typical office environment. The birth-death property of MPC clusters and the non-stationarity over the antenna array were verified. In [13], the authors performed a measurement campaign in an outdoor environment at the center frequency of 15 GHz with a bandwidth of 4 GHz by utilizing a virtual 40×40 planar antenna array. The authors introduced the spatial-stationary clusters and described their behaviors such as the life distance in horizontal and vertical directions.

On the other hand, channel polarization characteristics have drawn attention from the 4G to 5G. The authors in [14] presented the models to describe the dependence of cross-polarization discrimination (XPD) on distance, angular spreads, and DS in the 3D MIMO cross-polarized channels. The authors in [15] parameterized an MPC cross-polarization ratio (XPR) model for the indoor and outdoor environments in the above-6G bands based on 28 measurement campaigns. They found that XPR did not depend strongly on frequency or environment. The authors in [16] performed measurements in a small office and an entrance hall at 70 to 77 GHz utilizing a 3D spherical virtual antenna array. They presented a double-directional dual-polarimetric MIMO channel model in which the polarimetric statistics were highly correlated and exhibited a clear dependence on the geometry of environments. For sub-6G bands, the authors in [17] performed measurement at 5.3 GHz with dual-polarization in an urban street and also used the ray-tracing method to study the polarimetric behaviors.

The latest 3GPP release TR 36.873 [3] has specified the channel models that consider both the horizontal and vertical directions. The models will support evaluating the performance of physical-layer and higher-layer techniques in various scenarios. The 3.5 GHz carrier frequency is proposed for heterogeneous networks in [3]. For the UMa scenario, the distributions of AoA and EoA are modeled by the wrapped Gaussian and Laplacian distributions, respectively, and the delay distribution is described by the exponential distribution. The cluster power in PDPs is modeled by exponential decaying distribution and the composite cluster APS and EPS are modeled by the wrapped Gaussian and Laplacian distribution, respectively. IMT-2020 in [18] gives similar conclusions with the 3GPP standards. PDP can be approximated by an

exponential decaying function, and the Gaussian and Laplacian functions are adopted for APS and EPS, respectively. The METIS project in [19] has specified some new requirements for 5G and meanwhile proposed the approach including a map-based, stochastic and hybrid models to provide a flexible and scalable channel modelling framework.

Different from the previous works, in our measurement campaign, we emulated the deployment of a BS and UEs in a typical UMa O2I scenario at 3.5 GHz, the candidate 5G frequency. The spatial and temporal multipath propagation in cross polarizations in this scenario has not been sufficiently explored. In particular, we investigate the propagation parameters in the space, time, and polarization domains simultaneously and the clustering behavior. Thus we can describe the propagation in multiple domains more accurately and also reveal the impact of polarization on the channel characteristics in more depth. Furthermore, the cluster-based stochastic channel models for both the spatial and temporal propagation profiles can extend the existing channel model standards such as the 3GPP and METIS specifications.

III. CHANNEL PROPAGATION PARAMETERS AND PROFILES

For purpose of describing the 3D multipath propagation in radio channels, we adopt the spatial-temporal channel impulse response (CIR) model that includes the AoA, EoA, and excess delay information of MPCs. The CIR model is expressed as

$$h(\tau, \theta, \phi) = \sum_{l=1}^L \alpha_l e^{j\psi_l} \delta(\tau - \tau_l, \phi - \phi_l, \theta - \theta_l), \quad (1)$$

where L is the number of signal propagation paths (*i.e.*, MPCs), $\alpha_l e^{j\psi_l}$, τ_l , ϕ_l , and θ_l are the complex gain, excess delay, AoA, and EoA of the l -th path, respectively. The delta function $\delta(\tau, \theta, \phi)$ represents an impulse at the excess delay of 0 ns and incident angle of $(0^\circ, 0^\circ)$ in the joint space-and-time domain. These parameters for individual MPCs are the *small-scale parameters*.

The *large-scale parameters* describe the characteristics of the MPC set in a CIR. In the space domain, RMS ASA and ESA describe the angular dispersivity of the power arrival over the impinging directions in the azimuth and elevation dimensions, respectively. ASA is denoted by S_A and calculated by

$$S_A = \sqrt{\frac{\sum_{l=1}^L \alpha_l^2 (\phi_l - \mu_A)^2}{\sum_{l=1}^L \alpha_l^2}}, \quad (2)$$

where μ_A is the power weighted mean of AoA and defined as

$$\mu_A = \frac{\sum_{l=1}^L \alpha_l^2 \phi_l}{\sum_{l=1}^L \alpha_l^2}. \quad (3)$$

ESA, denoted by S_E , is defined in a similar form with ϕ_l replaced by θ_l in (2) and (3). In the time domain, RMS DS describes the spread of the power arrival over the

excess delay. DS, denoted by S_D , is calculated similarly with respect to τ_l .

For the propagation profiles in the space domain, APS and EPS present the distribution of the power arrival over the incident angles in the horizontal and vertical planes, respectively. The APS between a pair of TX and RX, denoted by $p_A(\phi)$, is defined as

$$p_A(\phi) = \sum_{l=1}^L |\alpha_l|^2 \delta(\phi - \phi_l). \quad (4)$$

EPS, denoted by $p_E(\theta)$, is defined similarly for EoA, θ_l . PDP describes the MPC arrival with respect to excess delay. PDP, denoted by $p_D(\tau)$, is defined similarly by (4) where the independent variable is replaced by the excess delay of MPCs.

We evaluate the correlation between $\pm 45^\circ$ polarized channels by calculating the cross-correlation of the channel profiles. For APS, the variable of ϕ can be discretized by the interval of 1° in practical channel measurement. Thus the measured APS is a discrete sequence with respect to the index of AoA. When the transmitting antenna is in $+45^\circ$ polarization, the signal is $+45^\circ$ polarized (for easy presentation, the radio channel is called $+45^\circ$ polarized channel) and the APS sequence is denoted by $\mathbf{p}_A^+(k)$ where k is the index of the AoA bins. Similarly, the APS sequence in the -45° polarized channel is denoted by $\mathbf{p}_A^-(k)$. Then the cross-correlation coefficient for APS is expressed as

$$\rho_C = \frac{\text{cov}[\mathbf{p}_A^+(k), \mathbf{p}_A^-(k)]}{\sqrt{\text{var}[\mathbf{p}_A^+(k)]} \sqrt{\text{var}[\mathbf{p}_A^-(k)]}}. \quad (5)$$

The cross-correlation for EPS is defined similarly where the EPS sequences are defined with respect to the discrete EoA (e.g., with the interval of 1°). We discretize the PDPs by the delay bin and thus obtain the PDP sequences, denoted by $\mathbf{p}_D^+(k)$ and $\mathbf{p}_D^-(k)$, where k is the index of the delay bins.

IV. CHANNEL MEASUREMENT SCENARIO AND SYSTEM

A. MEASUREMENT SCENARIO

The measurement campaign was conducted in a modern business district. The TX emulated a BS and was installed on the rooftop of 5-storey building where the antenna array was 25 meters above the ground. The RX was used to emulate UEs distributed inside a building. The RX system was stacked on an electric trolley and moved to eight positions along the corridors on the 1st, 2nd, and 3rd floors in another office building. The RX positions were spaced by 1.5 meters. The building walls were made by concrete and there were glazed windows in the external walls of the corridors. The farthest distance between the TX and RX was about 200 meters. The positions of the TX and RX are marked on the building floorplan in Fig. 1. Fig. 2 shows the TX and RX systems and the measurement environment. The line of sight (LOS) propagation path between the TX and RX was blocked by a glazed window or a concrete external wall. The trees and shrubberies out of the windows may also be obstacles when the RX was on the first floor. Since there were no people walking around

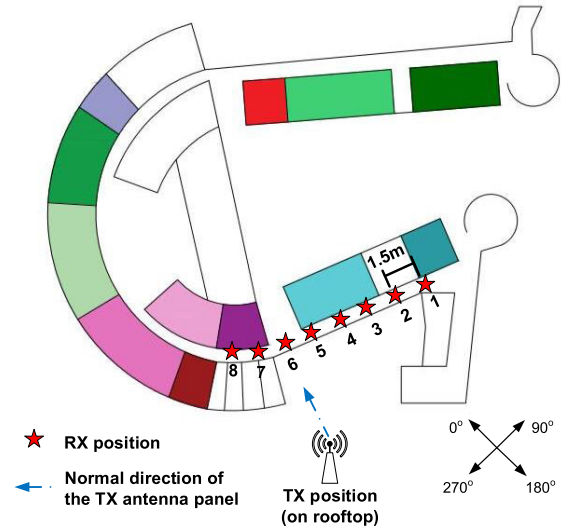


FIGURE 1. Floorplan of the measurement building and the positions of the TX and RX.

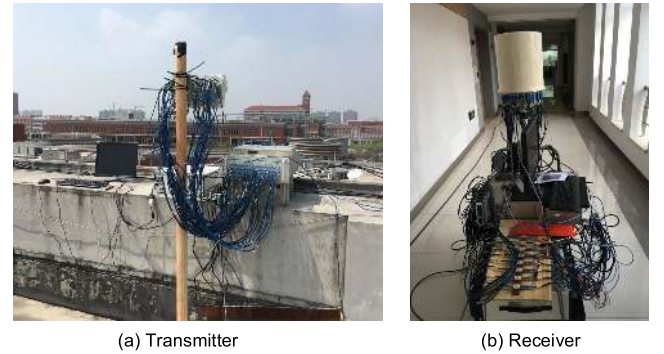


FIGURE 2. Channel sounder.

in the corridors, the channels in the corridors were static. This measurement setting emulated the typical O2I network converge in the 5G system.

B. MEASUREMENT SYSTEM

We used a 3D-MIMO radio channel sounder as shown in Fig. 2. The sounder employs the direct sequence spread spectrum (DSSS) scheme to probe channels and detect the propagation of MPCs. The probing signal is a pseudo-noise (PN) sequence composed of 1,023 chips. The signal bandwidth is 160 MHz and thus the chip duration (i.e., the delay bin in the measured temporal CIRs) is 6.25 ns. Six repeats of the PN sequences plus additional prefix and suffix chips form a channel probing frame (CPF) with the length of 6,400 chips. Thus the duration of a CPF is $6400/(160 \times 10^6) \times 10^6 = 40 \mu s$.

The TX uses a rectangular planar array (RPA) of 32 patches in a 4×8 matrix. Each patch contains two cross-polarized ($\pm 45^\circ$) dipole antennas and the 64 dipoles in the RPA form two arrays in $\pm 45^\circ$ polarizations. Each dipole has 3 dBi gain and a half power beam from -60° to $+60^\circ$ in both the azimuth and elevation dimensions with respect to the normal direction. The spacing distance between adjacent patches is half a wavelength for the 3.5 GHz carrier wave. In the

TX system, an arbitrary waveform generator (AWG) generates the CPFs circularly and input the sequences into an vector signal modulator. The CPFs are modulated via BPSK on the carrier of 3.5 GHz frequency. Then, after passing through a power amplifier, the modulated radio signal is sent to a 1-input-64-output microwave switch (MS). The output ports of the MS are connected to the 64 dipoles in the RPA. The MS routes the input channel sounding signal to one of the output ports to transmit the signal on one dipole. The MS selects one output port for 320 μ s and then switches to the next port. Thus each dipole transmits eight CPFs in a time slot and the dipoles in the RPA transmit one-by-one circularly. The process that all the 64 dipoles transmit eight CPFs each is called a *transmitting cycle*.

The RX utilizes an omnidirectional cylindrical array (OCA) that comprises 32 patches of $\pm 45^\circ$ polarized dipoles. The patches are placed in 8 columns that form a cylinder and each column has 4 patches. The dipoles are connected to the input ports of a 64-input-8-output MS. The MS captures the signals on the 8 dipoles in one column for a time slot of 40 μ s (the duration of one CPF) and then switch to the next column. In this way, the signals are captured column-by-column circularly by the RX. The process that the signals on all the dipoles in the OCA are captured for one round is called a *receiving cycle*. The duration of a receiving cycle is $8 \times 40 = 320 \mu$ s. Thus while one TX dipole antenna is transmitting, the RX can complete a receiving cycle. The output signals from the MS (the signals on the 8 dipoles in a column) are input into the low noise amplifiers (LNA) and bandpass filters and then into a multi-channel vector signal receiver (MC-VSR). The MC-VSR samples and digitalizes the radio signals at the sampling rate of 200 MHz, and the sample data of the I/Q components are stored in hard disks for off-line processing.

The TX and RX systems are both equipped with a GPS-triggered rubidium clock (RC). The RCs generate synchronized one pulse per second (PPS) clocks to the AWG, MSs, and MC-VSR to start the signal transmission and capture simultaneously at the beginning of every second. The RCs also output synchronized 10 MHz clocks to the two MSs to switch the antennas synchronously, in order to ensure that the RX captures the signals on the dipoles at the beginning of each CPF.

When a dipole antenna in the TX RPA transmits for 320 μ s, the RX OCA completes a receiving cycle and each antenna captures the channel response of a CPF. The received array signal on the OCA from a transmitting antenna to the 64 antennas, form two 1×32 MIMO channel responses for $\pm 45^\circ$ polarizations. The array signal received on the 32 antennas in one polarization is called a *channel snapshot*. We can extract MPCs and obtain the parameter sets of the MPCs and propagation profiles using the method described as follows.

The MPCs in the received signals on each RX antenna are identified by sliding correlation and spatial-smoothing method in the joint time and space domains. The AoA and EoA of every resolved MPC are determined using the

complex responses on the RX OCA and the 2-dimensional direction-of-arrival estimation algorithm [20] [21]. Before the measurement campaign, we have measured the 3D radiation pattern of the PRA and OCA with the angular resolution of 1° . The measured steering vectors are plugged into the angular parameter estimation algorithm such that the effect of the antenna responses is removed. In addition, the phase shifts of the radio chains in the RX system are measured by connecting the TX and RX directly with cables on every measurement day. These system phase shifts are removed from the captured complex array signals before direction-of-arrival estimation.

C. MEASUREMENT DATA STRUCTURE

In this measurement campaign, when the RX was at a position, the sounder completed a transmitting cycle to measure the channel. Since there were 32 antennas in one polarization in the RPA on the TX, we obtained 32 channel snapshots (*i.e.*, 32×32 MIMO channel responses, as specified in Sec. IV-B) in one polarization.

The MPCs in a channel snapshot are resolved and the small-scale parameters of each MPC are estimated using the method described in Sec. IV-B. In a measured CIR, we set the threshold of $P_{M,th} = \max\{P_1, P_2\}$ where P_1 is the signal power with -25 dB attenuation from the most significant path and P_2 is the power level with 2 dB above the noise power. A propagation path is a valid MPC only when its power is larger than $P_{M,th}$. According to channel model in Sec. III, we have obtained the measurement results from every channel snapshot including

- the MPC number (denoted by \hat{L}),
- the small-scale parameter sets of all the MPCs (denoted by $\hat{\Omega}_l = \{\hat{\alpha}_l, \hat{\psi}_l, \hat{\tau}_l, \hat{\phi}_l, \hat{\theta}_l\}$ for $l = 1, 2, \dots, L$),
- the large-scale channel parameters of ASA, ESA, and DS (denoted by \hat{S}_A, \hat{S}_E , and \hat{S}_D , respectively),
- the propagation profiles of APS, EPS, and PDP (denoted by $\hat{p}_A(\phi)$ for $\phi \in [0^\circ, 360^\circ)$, $\hat{p}_E(\theta)$ for $\theta \in [0^\circ, 180^\circ)$, and $\hat{p}_D(\tau)$ for $\tau \in [0, \tau_{\max}]$ where τ_{\max} is the maximal excess delay).

The TX and RX were stationary during measurement when the RX was placed at a position. There was not large-scale fading among the 32 snapshots in one polarization in a transmitting cycle because the scattering environment did not change. But the noise in the sounder system and channel as well as the subtle change in the environment may cause random variation in the measured MPCs. As an illustrative example, the APSs and EPSs in the 32 snapshots at the 2nd RX position on the 3rd floor are presented in Fig. 3. We can see that the incident angles and power of the significant MPCs with relatively large power are stable among the 32 snapshots and the less significant MPCs vary randomly. Therefore, without large-scale fading, the MPC parameters in a transmitting cycle follow the same probability distributions (*i.e.*, the measurement results are from the same sample space).

We take the average APS, EPS, and PDP from the 32 snapshots in a transmitting cycle as the measured

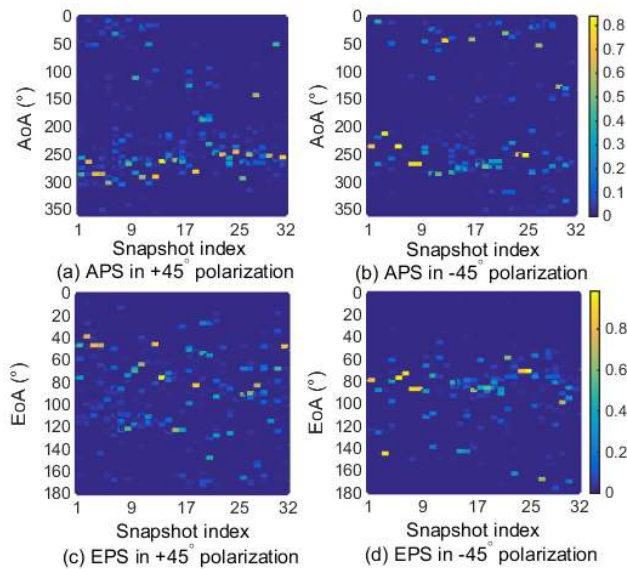


FIGURE 3. The measured APSs and EPSs in one transmitting cycle at the RX Position 2 on the 3rd floor. The x-axes are the index of the transmitting dipole in the TX.

propagation profiles for a RX position to remove the random variation caused by noise. We calculate the large-scale fading parameters from the average propagation profiles for every RX position. Then we collect the large-scale fading parameter values at all the RX positions together to obtain the statistical distributions of the parameters. Meanwhile, we find the best-fitting models with certain parameter values for the propagation profiles at each RX position. Then based on the model parameters at all the RX positions, we obtain the statistical distributions of the model parameters for the propagation profiles.

V. MEASUREMENT RESULTS AND STATISTICAL MODELS FOR SPATIAL PROPAGATION

A. MEASUREMENT RESULTS OF APS

At every RX position, we obtained two average APSs in $\pm 45^\circ$ polarizations. Fig. 4 presents the measured APSs at RX Position 2 on the 1st, 2nd, and 3rd floors. Multiple distinct clusters in every APS illustrate the evident clustering behavior of MPCs in the azimuth dimension. We can observe several important phenomena in Fig. 4.

First, the main (most significant) clusters in the APSs generally arrived at the RX from the direction of the TX, and hence should be formed by the MPCs directly penetrating the glazed windows or external walls. As shown in Figs. 4(a), (b), (e), and (f) for the 1st and 3rd floors, the main clusters are located at about 250° , the direction of the TX, according to the space coordinate in the measurement.

Second, the other clusters should be generated by the reflections of the walls and grounds of the corridors. The reflection processes of the MPCs are illustrated in Fig. 5(a) for the azimuth dimension. For example, several clusters arrive with the AoAs from 50° to 100° on the 1st floor as

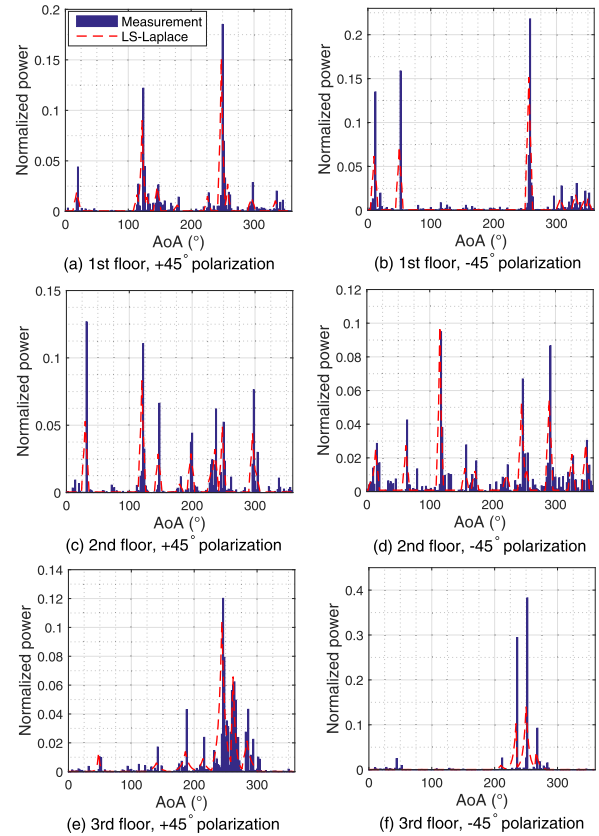


FIGURE 4. Measured APSs at RX Position 2 on the three floors and the fitting LS-Laplace functions.

shown in Figs. 4(a) and (b). These clusters may be reflected by the walls behind the RX and hence propagate to the RX on the other side with respect to the TX.

Third, the clustering behavior on the 2nd floor is different, as shown in Figs. 4(c) and (d). The main clusters arrive at the direction of about 120° . This is because there is rich foliage outside the 2nd floor that blocks the direct LOS propagation path severely. Meanwhile, there is a metal door behind the RX in the corridor that generates a strong reflection cluster. In addition, as we can observe in the figures, there are much more reflected clusters in the APS due to the foliage and metal objects around the RX on the 2nd floor.

Fourth, the measured APSs in $\pm 45^\circ$ polarizations are quite similar with each other on every floor. This indicates that the spatial propagation profiles in the cross-polarized channels are consistent and polarization does not affect considerably the statistical characteristics.

B. MEASUREMENT RESULTS OF EPS

The two measured EPSs in $\pm 45^\circ$ polarizations at the RX Position 2 on the three floors are shown in Fig. 6. We can see that the MPCs also arrive at the RX in distinct clusters in the elevation dimension. We have several important observations as follows.

First, the numbers of EPS clusters are obviously fewer than those in the APSs. The MPCs are more concentrated in the main cluster at the LOS direction in an EPS. The reason

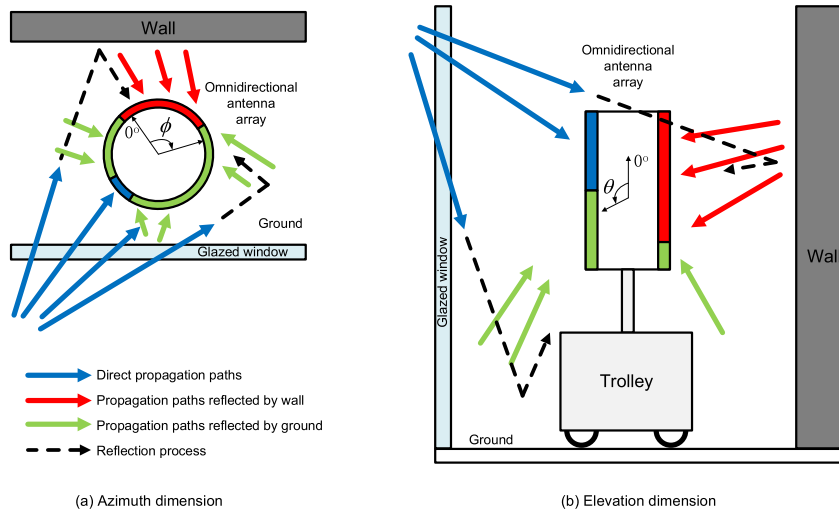


FIGURE 5. Diagrammatic sketches for MPC reflection in the azimuth and elevation dimensions in the corridor environment.

can be explained using the sketch in Fig. 5(b). When the MPCs are reflected on the walls, their EoAs are close to the direct propagation path penetrating the glazed windows or external walls. Second, the clusters with EoAs larger than 90° should be mainly generated by the ground reflection. Third, there are obviously more clusters that distribute over the EoA range on the 2nd floor, as shown in Figs. 6(c) and (d). This phenomenon is consistent with the APSs and because of the more complicated scattering environments with rich foliage and metal objects around on the 2nd floor. Fourth, the EPSs in $\pm 45^\circ$ polarizations are similar with each other. This reveals that the polarization does not affect the statistical characteristics of the MPC propagation in the elevation dimension.

C. STATISTICAL MODELING OF APS

According to the analysis in Sec. V-A, an APS can be divided into three parts: a main (the most significant) cluster at the direct propagation direction, the other significant clusters generated by ground and wall reflections, and the scattered MPCs by scattering in the surrounding environments. The process to establish the model for APS in this work includes three steps. First, we select an appropriate function to model the profile of APS including both the clusters and scattered MPCs. Second, we locate the clusters and find the optimal modeling parameters. Third, the distributions of the parameters in the APS model are determined based on our measured APS samples.

1) MODELING FUNCTION OF APS

First, we determine the modeling function for the power spectra of the main clusters in the APSs. Let $\mu_{A,1}$ denote the angular location of the main cluster in an APS. Since the center of the main cluster should be at the AoA of the maximum power, $\mu_{A,1}$ is determined by $\mu_{A,1} = \arg\max_{\phi \in [0^\circ, 360^\circ)} \{\hat{p}_A(\phi)\}$. The power spectrum inside a cluster should keep reducing monotonously and be larger than the threshold $P_{M,th}$.

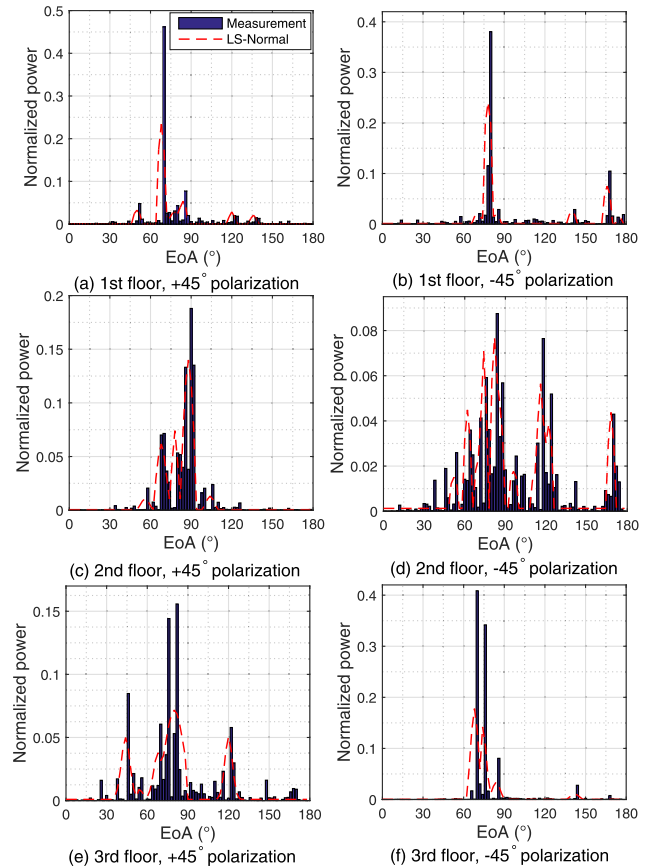


FIGURE 6. Measured EPSs at RX Position 2 on the three floors and the fitting LS-Laplace functions.

Therefore the angular boundaries of the main cluster are the AoAs of adjacent local peaks or the direction with power equal to $P_{M,th}$. Suppose that the AoA range of the main cluster is $[\phi_L, \phi_U]$. According to the shapes of the main clusters (e.g., as shown in Fig. 4), we choose the truncated Laplace,

TABLE 1. RMSEs of curve fitting for APS and EPS main clusters.

Fitting Model	APS		EPS	
	+45°	−45°	+45°	−45°
Truncated power-scaled Laplace	0.0194	0.0192	0.0319	0.0307
Truncated power-scaled Cauchy	0.0202	0.0195	0.0312	0.0302
Truncated power-scaled Normal	0.0199	0.0198	0.0308	0.0298

Cauchy, and normal distribution PDFs to fit the main clusters. Meanwhile, because the measured APSs are normalized and the power of each cluster is less than one, we introduce a power parameter, a_A , into the candidate functions to scale the total power in fitting the main clusters.

The root-mean-square-error (RMSE) of the candidate function, denote by $f_C(\phi)$, in fitting the power spectra is

$$\varepsilon = \frac{1}{\phi_U - \phi_L} \int_{\phi_L}^{\phi_U} [f_C(\phi) - \hat{p}_A(\phi)]^2 d\phi. \quad (6)$$

We have obtained a total of 48 APSs in $\pm 45^\circ$ polarizations at the 24 RX positions in this measurement campaign. We fit the candidate functions to the main clusters in all the APSs and the average RMSEs of the 24 APSs in one polarization for each candidate function are listed in Table 1. Because the truncated power-scaled Laplace distribution PDF has the minimum RMSEs in both polarizations, we select it as the modeling function for the clusters in APSs. The fitting function for a cluster at μ is expressed as

$$f_{Lap}(\phi) = \frac{a}{2b} \exp\left[-\frac{|\phi - \mu_{A,1}|}{b}\right], \quad \phi \in [0^\circ, 360^\circ] \quad (7)$$

where a and b are the power and scale parameter, respectively.

Second, we employ $f_{Lap}(\phi)$ to model the other clusters. Suppose that there are I_A significant clusters in an APS, the parameters of $f_{Lap}(\phi)$ for the i -th cluster are denoted by $\mu_{A,i}$, $a_{A,i}$, and $b_{A,i}$ for $i = 1, 2, \dots, I$. The determination of these parameters will be discussed in details in the next subsection.

Third, since the scattered MPCs arrive at the RX at omnidirectional azimuth angles, we introduce a constant power floor in the APS model to describe the uniform arrival of the scattered MPC over the AoA range. Because the total power of the significant clusters are $\sum_{i=1}^{I_A} a_{A,i}$, the angular power density for the scattered MPCs is $(1 - \sum_{i=1}^{I_A} a_{A,i})/360$.

In summary, we propose a cluster-based model for APS, called *lifted-superposed Laplace distribution (LS-Laplace)* function. The model is expressed as

$$f_{APS}(\phi) = \sum_{i=1}^{I_A} \frac{a_{A,i}}{2b_{A,i}} \exp\left[-\frac{|\phi - \mu_{A,i}|}{b_{A,i}}\right] + \frac{(1 - \sum_{i=1}^{I_A} a_{A,i})}{360}, \quad \phi \in [0^\circ, 360^\circ] \quad (8)$$

where $(1 - \sum_{i=1}^{I_A} a_{A,i})/360$ is the power floor formed by the scattered MPCs. We can ensure that the total power of $f_{APS}(\phi)$ is normalized because $\int_0^{360} f_{APS}(\phi) d\phi = 1$. The LS-Laplace function combines the power-scaled truncated Laplace distribution PDFs for the significant clusters and the power floor for the scattered MPCs together. The modeling functions for the APSs are also plotted in Fig. 4.

2) LOCALIZATION AND MODELING OF CLUSTERS

As described above, we have located and modeled the main clusters in the APSs with the function $f_{Lap}(\phi)$. Without loss of generality, the index of the main cluster in an APS is $i = 1$. Thus, we have obtained the values of the parameters of $\mu_{A,1}$, $a_{A,1}$ and $b_{A,1}$ for each measured APS.

Furthermore, we propose an algorithm to identify all clusters in the measured APSs. At first, we use a threshold to determine the existence of a significant cluster that is

$$P_{C,th} = \overline{\hat{p}_A(\phi)} + \hat{\sigma}_A, \quad (9)$$

where $\overline{\hat{p}_A(\phi)}$ and $\hat{\sigma}_A$ are the average power and standard deviation (STD) of $\hat{p}_A(\phi)$, respectively. When the APS power is larger than $P_{C,th}$ at a certain AoA, there may be a cluster at the direction with its center at this AoA.

Then we propose an iteration algorithm to identify and model the clusters in an APS, as given in Algorithm 1. The input parameters are the measured APS, parameters of $f_{Lap}(\phi)$ for the main cluster, and the power threshold given in (9). The output results are the number of significant clusters and the parameters of $f_{Lap}(\phi)$ for the other clusters.

Algorithm 1 Searching and Modeling for Clusters in an APS

Input: $\hat{p}_A(\phi)$, $\mu_{A,1}$, $b_{A,1}$, and $P_{C,th}$;

Output: I_A , $\mu_{A,i}$, $a_{A,i}$, and $b_{A,i}$ ($i = 2, 3, \dots, I$);

- 1: Set $i = 1$;
- 2: Set $\hat{p}_A(\phi) = 0$ for $(\mu_{A,1} - \sqrt{2}b_{A,1}) \leq \phi \leq (\mu_{A,1} + \sqrt{2}b_{A,1})$;
- 3: **while** $\max\{\hat{p}_A(\phi) | \phi \in [0^\circ, 360^\circ]\} \geq P_{th}$ **do**
- 4: $i = i + 1$;
- 5: Get $\mu_{A,i} = \operatorname{argmax}_{\phi \in [0^\circ, 360^\circ]} \{\hat{p}_A(\phi)\}$;
- 6: Set $\hat{p}_{AC,i}(\phi) = \hat{p}_A(\phi)$ for $(\mu_{A,i} - \sqrt{2}b_{A,1}) \leq \phi \leq (\mu_{A,i} + \sqrt{2}b_{A,1})$;
- 7: Fit $\hat{p}_{AC,i}(\phi)$ by $f_{Lap}(\phi)$ in (7) using the minimal RMSE criteria, and get $a_{A,i}$ and $b_{A,i}$.
- 8: Set $\hat{p}_A(\phi) = 0$ for $(\mu_i - \sqrt{2}b_1) \leq \phi \leq (\mu_i + \sqrt{2}b_1)$;
- 9: **end while**
- 10: Set $I_A = i$.

We first remove the main cluster over the angular range of $[\mu_{A,1} - \sqrt{2}b_{A,1}, \mu_{A,1} + \sqrt{2}b_{A,1}]$ from the APS in Step 2. We approximate the angular range of the main cluster by $2\sqrt{2}b_1$ where $\sqrt{2}b_{A,1}$ is the STD of the fitting function. In Step 5, we find the center of the next significant cluster, $\mu_{A,i}$, that has the maximum arriving power in the current APS. As we can observe in Fig. 4, the angular spreads of the clusters are similar with that of the main cluster in an APS. Therefore, we extract the measured power spectrum over the AoA range of $[\mu_{A,i} - \sqrt{2}b_{A,1}, \mu_{A,i} + \sqrt{2}b_{A,1}]$ in Step 6 and fit the cluster power spectrum, $\hat{p}_{AC,i}(\phi)$, by $f_{Lap}(\phi)$ in Step 7. Then we remove the identified cluster from $\hat{p}_A(\phi)$ in Step 8 and go back to Step 3 to find the next cluster. The algorithm can find and model all the significant clusters sequentially by the iterative operation.

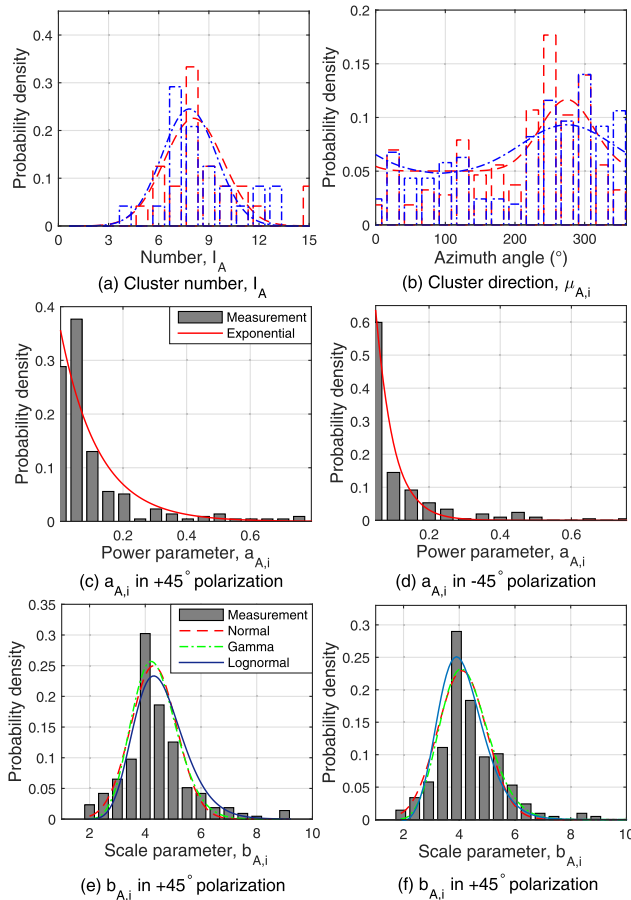


FIGURE 7. Frequency histograms and distribution PDFs of the parameters of the APS model. In (a) and (b), the histograms are the measurement results, and the curves are the fitting PDFs of the normal and LT-Normal distributions, respectively. The blue dotted-dashed and red dashed figures are for $+45^\circ$ and -45° polarizations, respectively.

3) DISTRIBUTIONS OF THE PARAMETERS IN THE LS-LAPLACE MODEL

By using Algorithm 1, we identify 422 significant clusters in the measured APSs in $\pm 45^\circ$ polarizations at the 24 RX positions, and obtain the values of the parameters of $a_{A,i}$, $b_{A,i}$, and $\mu_{A,i}$. Fig. 7 presents the frequency histograms of the parameters. The distributions of the parameters are determined based on these sample sets as follows.

- 1) The numbers of clusters, I_A , in the 48 measured APSs in $\pm 45^\circ$ polarizations are plotted in Fig. 7(a). We can see that the cluster numbers follow the normal distribution well. Therefore we model I_A as a normal random variable and the distribution parameters obtained by hypothesis test are listed in Table 2.
- 2) The distributions of the cluster directions (*i.e.*, the AoAs of the cluster centers, $\mu_{A,i}$) in $\pm 45^\circ$ polarizations are plotted in Fig. 7(b). Please note that the LOS direction is about 250° . As expected, the clusters have a higher probability to arrive around the LOS direction. The probability for clusters to occur within the AoA range of $[0^\circ, 220^\circ]$ is about 0.1 to 0.27, while the probability in the AoA range of $[220^\circ, 360^\circ]$ is from

0.21 to 0.6. Therefore, about 60% clusters arrive at the RX within 120° around the LOS direction. The clusters are generated by the direct propagation penetrating obstacles and the reflections by the ground and objects in front of the RX. The clusters in the other AoA ranges are mainly generated by the wall reflections behind the RX. The AoA range and number of these clusters are larger but their power is much smaller than the LOS cluster. Suggested by the empirical distributions in Fig. 7(b), we propose to use the truncated normal distribution with a constant probability floor, named lifted-and-truncated normal (LT-Normal) distribution, for $\mu_{A,i}$ in both $\pm 45^\circ$ polarizations. The PDF is expressed as

$$f_{LT}(\phi) = \frac{a_{\mu,A}}{\sqrt{2\pi}\sigma_{\mu,A}} \exp\left[-\frac{(\phi - \mu_{\mu,A})^2}{2\sigma_{\mu,A}^2}\right] + \frac{1 - a_{\mu,A}}{360}, \quad \phi \in [0^\circ, 360^\circ] \quad (10)$$

where $\frac{1 - a_{\mu,A}}{360}$ is the probability floor to represent the cluster arrival at omni-directional AoAs.

- 3) We utilize *exponential distribution* to model the power parameter, $a_{A,i}$, as shown in Figs. 7(c) and (d). In the measured APSs, the normalized power of most clusters is below 0.1. As mentioned earlier, we identify 422 significant clusters in the 48 APSs. Each APS has about 7 to 9 clusters and, considering the scattered MPCs, the average power of a cluster is about 0.1. However, since only a few most significant clusters contribute the majority of the received power, the power of the other clusters is well below 0.1. Therefore, the exponential distribution of the power parameter is reasonable. Meanwhile, the distribution of $a_{A,i}$ indicates that the power contribution by the scattered MPCs, $\frac{(1 - \sum a_{A,i})}{360}$, is unignorable and the power floor is necessary in the APS model. It is also revealed that the power arrival is quite dispersive in the azimuth dimension because of the numerous reflections and scattering in the UMa O2I scenario. The exponential distribution PDFs for the sample histograms are plotted in Figs. 7(c) and (d) and the distribution parameters are listed in Table 2.
- 4) The histograms of the scale parameter, $b_{A,i}$, are presented in Figs. 7(e) and (f). Suggested by the empirical distributions, we consider the candidate models of normal, lognormal, and Gamma distributions. The results show that the lognormal PDFs have the minimum RMSEs for both $\pm 45^\circ$ polarizations. The parameters of the lognormal distributions listed in Table 2. Since the parameter $b_{A,i}$ is around 4° , the angular spread of an APS cluster (the STD of the fitting) $f_{Lap}(\phi)$ is approximately $\sqrt{2}b_{A,i} \approx 5.7^\circ$.

In summary, from the measured 48 APSs in this campaign, we have obtained the LS-Laplace model for APS and the distributions of the model parameters for the UMa O2I scenario. The model is given in (8) and the parameter distributions are listed in Table 2.

TABLE 2. APS and EPS modeling parameters.

APS model: LS-Laplace function in (8)			EPS model: LS-Normal function in (11)		
Parameters	+45°	−45°	Parameters	+45°	−45°
$I_A \sim N(\mu_{I,A}, \sigma_{I,A})$	(8.10, 2.50)	(7.82, 2.30)	$J_E \sim N(\mu_{J,E}, \sigma_{J,E})$	(7.10, 3.40)	(7.26, 2.90)
$\mu_{A,i} \sim LT-N(\mu_{\mu,A}, \sigma_{\mu,A})$	(275, 53.80, 0.50)	(275, 93.20, 0.56)	$\mu_{E,j} \sim LT-N(\mu_{\mu,E}, \sigma_{\mu,E})$	(90, 38.00, 0.67)	(90, 64.10, 0.92)
$a_{A,i} \sim Exp(\mu_{a,A})$	0.40	0.38	$a_{E,j} \sim Exp(\mu_{a,E})$	0.35	0.33
$b_{A,i} \sim LnN(\mu_{b,A}, \sigma_{b,A})$	(1.63, 0.47)	(1.74, 0.52)	$\sigma_{E,j} \sim LnN(\mu_{\sigma,E}, \sigma_{\sigma,E})$	(2.39, 0.68)	(2.34, 0.68)

D. STATISTICAL MODELING OF EPS

1) MODELING FUNCTION OF EPS

Similar to the APSs, the EPSs also contain three parts: a main cluster at the direct propagation direction, the other significant clusters distributed over the incident angles, and the scattered MPCs, as shown in Fig. 6. Following the same approach for the APS modeling, we establish the EPS model by three steps.

First, to describe the clusters in EPS, we extract the main clusters from the 48 measured EPSs. According to the profiles of the EPS clusters, we select the truncated Laplace, Cauchy, and normal distribution PDFs to fit the power spectra of the extracted main clusters. Since the cluster power is smaller than one, we multiply the candidate functions by a power parameter, a_E . The RMSEs are listed in Table 1 and the truncated power-scaled normal distribution PDF, denoted by $f_{Nor}(\theta)$, has the minimum RMSEs in both $\pm 45^\circ$ polarizations.

Second, we locate and model all the clusters in the measured EPSs with $f_{Nor}(\theta)$, using Algorithm 1. The input parameters are the measured EPS, $\hat{p}_E(\theta)$, parameters for the main cluster, $\mu_{E,1}$ and $\sigma_{E,1}$, and the power threshold $P_{C,th}$. The output results are the number of significant clusters, J_E , and the parameters of $f_{Nor}(\theta)$ for the other clusters including $\mu_{E,j}$, $a_{E,j}$, and $\sigma_{E,j}$ for $j = 2, 3, \dots, J_E$. Please note that the angular range of an EPS cluster is approximated by $2\sigma_{E,1}$ in Algorithm 1.

Third, considering the scattered MPCs distributed over the EoA range, we introduce a constant power floor in the EPS model. The angular power density for the scattered MPCs is $(1 - \sum_{j=1}^{J_E} a_{E,j})/180$.

Finally, by combining the cluster fitting functions and constant power floor, we propose the EPS model called *lifted-superposed normal distribution (LS-Normal) function* that is expressed

$$f_{EPS}(\theta) = \sum_{j=1}^{J_E} \frac{a_{E,j}}{\sqrt{2\pi}\sigma_{E,j}} \exp\left[-\frac{(\theta - \mu_{E,j})^2}{2\sigma_{E,j}^2}\right] + \frac{1 - \sum_{j=1}^{J_E} a_{E,j}}{180}, \quad \theta \in [0^\circ, 180^\circ] \quad (11)$$

where $\frac{1 - \sum_{j=1}^{J_E} a_{E,j}}{180}$ is the power floor. We ensure the total power of $f_{EPS}(\theta)$ is normalized because $\int_0^{180} f_{EPS}(\theta) d\theta = 1$. The best-fitting LS-Normal functions are plotted in Fig. 6.

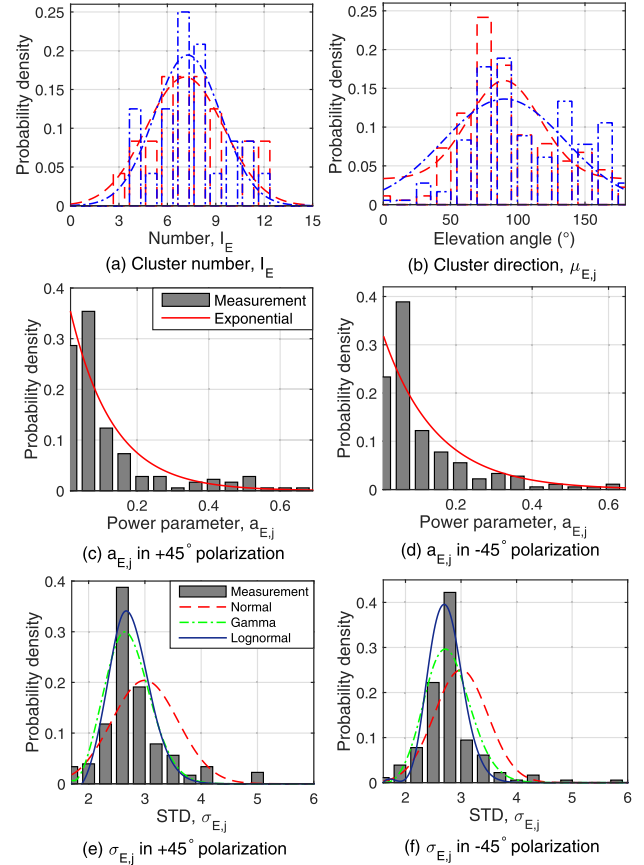


FIGURE 8. Frequency histograms and distribution PDFs of the parameters of the EPS model. In (a) and (b), the histograms are the measurement results, and the curves are the fitting PDFs of the normal and LT-Normal distributions, respectively. The blue dotted-dashed and red dashed figures are for +45° and −45° polarizations, respectively.

2) DISTRIBUTIONS OF THE PARAMETERS OF THE LS-NORMAL MODEL

From the 48 measured EPSs, we find 358 clusters and each cluster power spectrum provides a sample of $\mu_{E,j}$, $a_{E,j}$, and $\sigma_{E,j}$. The histograms of parameter samples are plotted in Fig. 8. The distributions of the model parameters are determined as follows. The selected distribution PDFs are plotted in Fig. 8 and the distribution parameters are listed Table 2.

- 1) The histogram of the cluster numbers, J_E , in the 48 measured EPSs in $\pm 45^\circ$ polarizations are plotted in Fig. 8(a). Using the hypothesis test, we model J_E

by the normal distribution and obtain the distribution parameters.

- 2) The distributions of the centers of the EPS clusters, $\mu_{E,j}$ in $\pm 45^\circ$ polarizations, are plotted in Fig. 8(b). The LOS direction is about 90° . About 70% significant clusters arrive in the EoA range from 60° to 120° . This distribution is similar with that of the APS clusters but is more concentrated. Meanwhile, we can see that more clusters arrive within the EoA of 90° to 180° than from 0° to 60° . The ground reflection is richer than the ceiling reflection, because the TX was higher than the RX in this O2I scenario. Similar with the model for $\mu_{A,j}$, we model $\mu_{E,j}$ with the LT-Normal distribution in (10) where the EoA range is $[0^\circ, 180^\circ]$.
- 3) The histograms of $a_{E,j}$ are plotted in Figs. 8(c) and (d). The measurement results suggest that $a_{E,j}$ in both $\pm 45^\circ$ polarizations has the lognormal distribution. Comparing with the exponential distribution of $a_{A,i}$ in the azimuth dimension, the EPS clusters tend to have more power than the clusters in the APSs. This may be because the significant MPCs (e.g., reflected by the ground) are more concentrated in the elevation dimension.
- 4) The STD, $\sigma_{E,j}$, also follow the lognormal distribution, as shown in Figs. 8(e) and (f). Most samples are smaller than 5° and smaller than $\sqrt{2}b_{A,i}$ in the azimuth dimension. This comparison also indicates that the power arrival in EPS clusters is more concentrated.

In summary, we have obtained the modeling function for EPS and the distributions of the model parameters for the UMa O2I scenario according to the measured 48 EPSs. The model is given in (11) and the parameter distributions are listed in Table 2.

E. STATISTICAL MODELS OF ASA AND ESA

Based on the measured APS and EPS in $\pm 45^\circ$ polarizations at each RX position, we calculate an ASA and ESA value utilizing (2). Thus we obtain 24 ASA and ESA samples in either polarization. Fig. 9 presents the frequency histograms of the samples in $\pm 45^\circ$ polarizations. Suggested by the shapes of the histograms, we consider five candidate distributions: lognormal, Gamma, Rayleigh, Weibull, and Nakagami distributions. According to the minimal RMSE criteria, we select the lognormal distribution to model both ASA and ESA in $\pm 45^\circ$ polarizations. The PDF for ASA is

$$f_{ASA}(s) = \frac{1}{\sqrt{2\pi}\sigma_{ASA}} \exp\left[-\frac{(\ln s - \mu_{ASA})^2}{2\sigma_{ASA}^2}\right], \quad (12)$$

where μ_{ASA} and σ_{ASA} are the mean and STD of ASA in the logarithmic domain. The lognormal model for ESA is defined similarly with the parameters of μ_{ESA} and σ_{ESA} . The value of the distribution parameters are listed in Table 3.

As shown in Figs. 9(a) and (b), the measured ASA has a high probability to be larger than 20° . The average ASA in this O2I scenario is larger than that of the outdoor NLOS

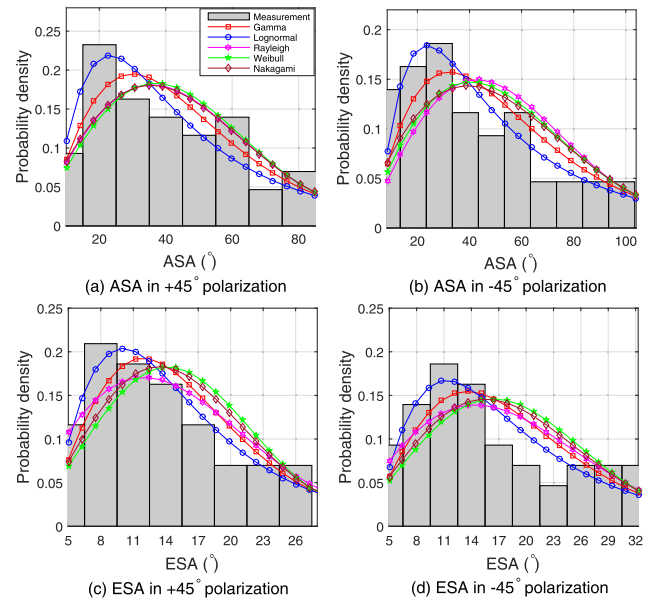


FIGURE 9. Frequency histograms and distribution PDFs of ASA and ESA.

TABLE 3. ASA and ESA modeling parameters.

Parameter	ASA		ESA	
	+45°	-45°	+45°	-45°
μ_{ASA}/μ_{ESA}	3.3397	3.4421	2.8047	2.9324
$\sigma_{ASA}/\sigma_{ESA}$	0.6740	0.8027	0.3404	0.3933

scenario [22]. This is due to the rich reflections in the indoor environment. The reflections from the ground and walls behind the RX leads to a large angular spread. As shown in Figs. 9(c) and (d), most of the ESA samples are in the range from 10° to 20° which is similar with the results in [23]. This is expected because of the similarity of the RX surrounding environments.

In addition, the means and STDs of the lognormal models for ASA and ESA in -45° polarization are both slightly larger than those in $+45^\circ$ polarization, as listed in Table 3. This indicates that the angular spread in the -45° polarized channel is larger and the power arrival is more dispersive. This phenomenon may be caused by the surfaces of the reflectors and scatterers in the propagation environments and the radio wave impinging directions on the objects. However, the difference is minor and the statistical characteristics in the cross-polarized channels are consistent.

VI. MEASUREMENT RESULTS AND STATISTICAL MODELS FOR TEMPORAL PROPAGATION

A. MEASUREMENT RESULTS OF PDPs

In this section, we investigate the channel characteristics in the time domain. Since we employed the PN-sequence of 1,023 chips to probe the channels, the sliding correlation of the received sounding signals with the PN-sequence provides the temporal CIR with 1,023 delay bins. It is observed that almost all the significant MPCs are within the 24 delay bins following the first significant MPC. Hence we choose the

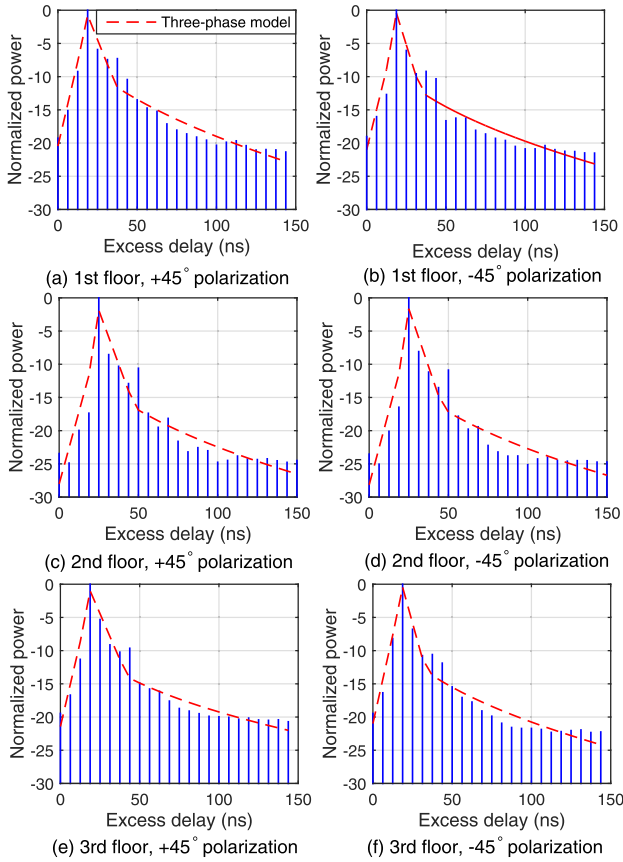


FIGURE 10. Measured PDPs and three-phase models at the 2nd RX position on each floor.

MPCs in the 24 delay bins in one CIR and thus the duration is $24 \times 6.25 = 150$ ns. From the 24 RX positions, we obtained 48 PDPs in $\pm 45^\circ$ polarizations, as described in Sec. IV-C. Fig. 10 presents the normalized PDPs at the 2nd RX position on each floor. We have two important observations.

First, the PDPs do not show clear clustering behavior and there is only a single decaying pattern in every PDP. The clustering behavior is not obvious comparing with those in the industrial scenario [24]. In addition, the APSs and EPSs have distinct clusters, as presented in Sec. V. This may be because in the O2I scenario, the RX is in a close space surrounded by walls and ceilings near by the RX. The significant MPCs arrive at the RX within a small excess delay range. Without sufficient differences in time of arrival, the clusters are overlapped with each other. Therefore we can distinguish the clusters in the APSs and EPSs in the space domain but cannot in the PDPs in the time domain.

Second, the largest power arrivals occur at about 20 to 25 ns in the PDPs. The first arriving MPC should be the direct propagation path penetrating the obstacles. However, some reflected MPCs arrive at the RX later and are superposed together, increasing the arrived power. Consequently, the superposition of the significant reflected MPCs generates power arrival that is larger than and lags behind the direct path.

TABLE 4. Distribution parameters of the parameters in the three-phase model.

Parameter	μ		σ	
	$+45^\circ$	-45°	$+45^\circ$	-45°
k_1	0.8176	0.7438	0.2660	0.3190
c_1	-18.2309	-19.4117	7.9705	7.1417
k_2	-0.7365	-0.6695	0.3519	0.2539
c_2	15.4782	15.4710	13.1131	10.3520
k_3	-3.1167	-3.1375	2.1213	2.2247
d	0.3846	0.3921	0.1728	0.1625

B. MODELING OF PDPs

According to the profiles in Fig. 10, an PDP can be divided into three phases: the rising, dropping, and trailing phases. First, the raising phase is from the beginning to the highest peak of the PDP (the maximum power arrival at about 25 ns). The power arrival during this phase should be formed by the MPCs through the direct propagation paths penetrating the obstacles and by the reflections on nearby walls and ground. Second, the arriving power begins to decrease quickly from the highest peak to the second peak (approximately at 50 ns). This period is the dropping phase during which the power is mainly from the significant MPCs reflected by the objects further away from the RX or reflected twice by nearby objects. Finally, beginning from the second peak, the PDP is in the trailing phase (approximately from 50 to 150 ns). In this phase, the PDP mainly comprises the scattered MPCs generated by the objects in the surrounding environment.

As suggested by the measured PDPs, we propose to use two linear functions to model the rising and dropping phases and a power function for the trailing phase to describe the gradual power attenuation. The segmented function of the three-phase model is expressed as

$$p_D(\tau) = \begin{cases} k_1 \tau + c_1, & \tau \in [0, \tau_H) \\ k_2 \tau + c_2, & \tau \in [\tau_H, \tau_S) \\ k_3 \tau^d, & \tau \in [\tau_S, \tau_{\max}] \end{cases} \quad (13)$$

where τ_H and τ_S are the excess delays of the highest and second peaks in the PDP, respectively. The best-fit functions are plotted in Fig. 10.

Since we collect 24 PDPs for one polarization at the RX positions, we obtain 24 samples of the parameters k_1 , k_2 , k_3 , c_1 , c_2 , and d for a polarization by fitting the PDPs. According to the hypothesis test, the samples follow the normal distribution well and the corresponding distribution parameters are listed in Table 4.

C. MEASUREMENT RESULTS AND MODELING OF DS

The DS for every RX position is calculated from the PDP as discussed in Sec. III. Fig. 11 presents the CDFs of the DS samples in $\pm 45^\circ$ polarizations at the 24 RX positions. In order to find the distribution of DS, we fit five CDFs of the lognormal, Gamma, Rayleigh, Weibull, and Nakagami distributions to the empirical CDFs.

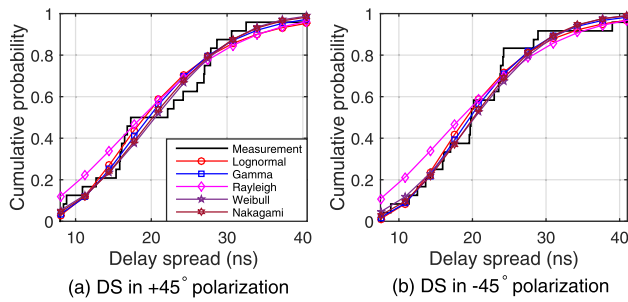


FIGURE 11. Empirical CDF and Candidate distributions for DS.

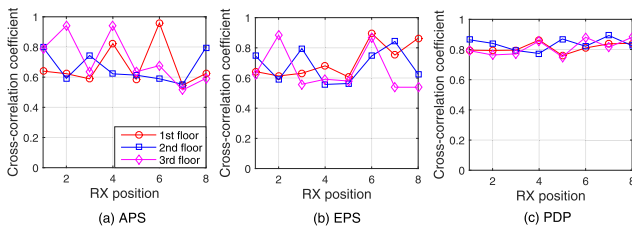


FIGURE 12. Correlation coefficients of the channel propagation profiles in $\pm 45^\circ$ polarizations.

The results show that the Rayleigh distribution has the minimum RMSEs in both $\pm 45^\circ$ polarizations. The PDF of the Rayleigh distribution for DS is expressed as

$$f_{DS}(s) = \frac{s}{\sigma_{DS}^2} \exp \left[-\frac{s^2}{2\sigma_{DS}^2} \right], \quad (14)$$

where σ_{DS} is the distribution parameter. The value of σ_{DS} for the $+45^\circ$ and -45° polarized channels is 15.87 and 15.48, respectively. The DSs in $\pm 45^\circ$ polarizations both follow the Rayleigh distribution and the parameters are quite similar.

VII. POLARIZATION CHARACTERISTICS OF THE UMA O2I CHANNELS

As presented in Secs. V and VI, the models for APS, EPS, and PDP are the same for $\pm 45^\circ$ polarizations and the model parameters have similar distributions. These results indicate that the clustering behaviors in the spatial and temporal propagation are consistent in the $\pm 45^\circ$ polarized channels. The models for ASA, ESA, and DS also indicate that polarization does not make considerable impact on the angular and delay spreads of the channels. Therefore, the statistical properties in both the space and time domains are consistent in $\pm 45^\circ$ polarizations.

In this subsection, we further compare the cross-polarized channels by evaluating the correlation between the APSs, EPSs, and PDPs in $\pm 45^\circ$ polarizations. The correlation coefficients at the 24 RX positions are calculated using (5) and plotted in Fig. 12. We can see that the correlation coefficients of the APSs and EPSs are from 0.6 to 0.9 and those of PDPs are from 0.75 to 0.9. The large correlation coefficients further indicate that the channel propagation profiles and statistical properties are consistent in $\pm 45^\circ$ polarizations.

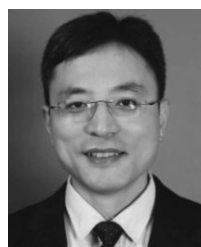
VIII. CONCLUSION

This paper presents a measurement campaign in a typical UMa O2I scenario at 3.5 GHz. The small and large-scale channel parameters and the multipath propagation profiles are obtained. The APS and EPS are modeled by the proposed LS-Laplace and LS-Normal functions, respectively, which include the significant clusters and power floor. The PDP is fitted by a three-phase model. The ASA and ESA follow the lognormal distribution and the DS has the Rayleigh distribution. We have also analyzed the reflection process of the MPC clusters in the O2I environment. The propagation profiles and statistical characteristics in $\pm 45^\circ$ polarizations are coincident, indicating that polarization does not make a significant impact. The statistical propagation models proposed in this paper are established based on the field channel measurement data. Therefore the models can be a reference for the design and deployment of the 5G network in the UMa O2I scenario. The propagation characteristics in the 5G spectrum in various scenarios are still less explored and more field channel measurements are required in future works. We also plan to apply our radio propagation model to 5G system simulations and analyze the sensitivity of network coverage performance to various channel parameters.

REFERENCES

- [1] E. G. Larsson, O. Edfors, F. Tufvesson, and T. L. Marzetta, "Massive MIMO for next generation wireless systems," *IEEE Commun. Mag.*, vol. 52, no. 2, pp. 186–195, Feb. 2014.
- [2] R. Zhang, Z. Zhong, J. Zhao, B. Li, and K. Wang, "Channel measurement and packet-level modeling for V2I spatial multiplexing uplinks using massive MIMO," *IEEE Trans. Veh. Technol.*, vol. 65, no. 10, pp. 7831–7843, Mar. 2016.
- [3] *Study on 3D Channel Model for LTE (Release 12)*, document TR 36.873 V12.4.0, 3GPP Technical Specification Group Radio Access Networks, Mar. 2017.
- [4] Y. Xiao, X. Du, J. Zhang, and S. Guizani, "Internet protocol television (IPTV): The killer application for the next generation Internet," *IEEE Commun. Mag.*, vol. 45, no. 11, pp. 126–134, Nov. 2007.
- [5] A. Kammoun, H. Khanfir, Z. Altman, M. Debbah, and M. Kamoun, "Preliminary results on 3D channel modeling: From theory to standardization," *IEEE J. Sel. Areas Commun.*, vol. 32, no. 6, pp. 1219–1229, Jun. 2014.
- [6] V. Kristem, S. Sangodoyin, C. U. Bas, M. Kaske, J. Lee, C. Schneider, G. Sommerkorn, J. Zhang, R. Thoma, and A. F. Molisch, "3D MIMO outdoor to indoor macro/micro-cellular channel measurements and modeling," in *Proc. IEEE Global Commun. Conf. (GLOBECOM)*, San Diego, CA, USA, Dec. 2015, pp. 1–6.
- [7] X.-Y. Wang, B. Li, X. Yuan, J.-W. Dou, and Y. Li, "Elevation angle research in three-dimension channel model using ray-tracing," in *Proc. URSI Gen. Assembly Sci. Symp. (URSI GASS)*, Beijing, China, Aug. 2014, pp. 1–4.
- [8] C. A. L. Diakhate, J.-M. Conrat, J.-C. Cousin, and A. Sibille, "Millimeter-wave outdoor-to-indoor channel measurements at 3, 10, 17 and 60 GHz," in *Proc. Eur. Conf. Antennas Propag. (EuCAP)*, Paris, France, Mar. 2017, pp. 1798–1802.
- [9] R. Zhang, L. Cai, X. Lu, P. Yang, and J. Zhou, "Elevation domain measurement and modeling of UMa uplink channel with UE on different floors," in *Proc. Int. Conf. Comput., Netw. Commun. (ICNC)*, Garden Grove, CA, USA, Feb. 2015, pp. 679–684.
- [10] R. He, O. Renaudin, V. Kolmonen, K. Haneda, Z. Zhong, B. Ai, and C. Oestges, "A dynamic wideband directional channel model for vehicle-to-vehicle communications," *IEEE Trans. Ind. Electron.*, vol. 62, no. 12, pp. 7870–7882, Dec. 2015.
- [11] P. Tang, J. Zhang, Y. Sun, M. Zeng, Z. Liu, and Y. Yu, "Clustering in 3D MIMO channel: Measurement-based results and improvements," in *Proc. IEEE Veh. Technol. Conf. (VTC-Fall)*, Boston, MA, USA, Sep. 2015, pp. 1–6.

- [12] J. Huang, C.-X. Wang, R. Feng, J. Sun, W. Zhang, and Y. Yang, "Multi-frequency mmWave massive MIMO channel measurements and characterization for 5G wireless communication systems," *IEEE J. Sel. Areas Commun.*, vol. 35, no. 7, pp. 1591–1605, Jul. 2017.
- [13] J. Chen, X. Yin, X. Cai, and S. Wang, "Measurement-based massive MIMO channel modeling for outdoor LoS and NLoS environments," *IEEE Access*, vol. 5, pp. 2126–2140, 2017.
- [14] M. Shafi, M. Zhang, A. L. Moustakas, P. J. Smith, A. F. Molisch, F. Tufvesson, and S. H. Simon, "Polarized MIMO channels in 3-D: Models, measurements and mutual information," *IEEE J. Sel. Areas Commun.*, vol. 24, no. 3, pp. 514–527, Mar. 2006.
- [15] A. Karttunen, J. Järveläinen, S. L. H. Nguyen, and K. Haneda, "Modeling the multipath cross-polarization ratio for above-6 GHz radio links," 2018, *arXiv:1804.00847*. [Online]. Available: <https://arxiv.org/abs/1804.00847>
- [16] C. Ling, X. Yin, R. Müller, S. Häfner, D. Dupleich, C. Schneider, J. Luo, H. Yan, and R. Thomä, "Double-directional dual-polarimetric cluster-based characterization of 70–77 GHz indoor channels," *IEEE Trans. Antennas Propag.*, vol. 66, no. 2, pp. 857–870, Feb. 2018.
- [17] V. Degli-Esposti, V.-M. Kolmonen, E. M. Vitucci, and P. Vainikainen, "Analysis and modeling on co- and cross-polarized urban radio propagation for dual-polarized MIMO wireless Systems," *IEEE Trans. Antennas Propag.*, vol. 59, no. 11, pp. 4247–4256, Nov. 2011.
- [18] *The Prediction of the Time and the Spatial Profile for Broadband Land Mobile Services Using UHF and SHF Bands*, document Rec. P.1816, ITU, 2015.
- [19] A. Osseiran, F. Boccardi, V. Braun, K. Kusume, P. Marsch, M. Maternina, O. Queseth, M. Schellmann, H. Schotten, H. Taoka, H. Tullberg, M. A. Uusitalo, B. Timus, and M. Fallgren, "Scenarios for 5G mobile and wireless communications: The vision of the METIS project," *IEEE Commun. Mag.*, vol. 52, no. 5, pp. 26–35, May 2014.
- [20] R. Zhang, S. Wang, X. Lu, W. Duan, and L. Cai, "Two-dimensional DoA estimation for multipath propagation characterization using the array response of PN-sequences," *IEEE Trans. Wireless Commun.*, vol. 15, no. 1, pp. 341–356, Jan. 2016.
- [21] R. O. Schmidt, "Multiple emitter location and signal parameter estimation," *IEEE Trans. Antennas Propag.*, vol. AP-34, no. 3, pp. 276–280, Mar. 1986.
- [22] R. Zhang, X. Lu, J. Zhao, L. Cai, and J. Wang, "Measurement and modeling of angular spreads of three-dimensional urban street radio channels," *IEEE Trans. Veh. Technol.*, vol. 66, no. 5, pp. 3555–3570, May 2017.
- [23] R. Zhang, H. Xu, B. Li, Z. Zhong, and C. Li, "Elevation power spectrum measurement and interference analysis of UMa I2O uplink channels," in *Proc. Int. Conf. Comput., Netw. Commun. (ICNC)*, Honolulu, HI, USA, Feb. 2019, pp. 936–942.
- [24] Y. Ai, M. Cheffena, and Q. Li, "Power delay profile analysis and modeling of industrial indoor channels," in *Proc. Eur. Conf. Antennas Propag. (EuCAP)*, Lisbon, Portugal, Apr. 2015, pp. 1–5.



RUONAN ZHANG (S'09–M'10) received the B.S. and M.Sc. degrees from Xi'an Jiaotong University, Xi'an, China, in 2000 and 2003, respectively, and the Ph.D. degree from the University of Victoria, Victoria, BC, Canada, in 2010, all in electrical and electronics engineering.

He was an IC Design Engineer with Motorola Inc., and Freescale Semiconductor Inc., Tianjin, China, from 2003 to 2006. Since 2010, he has been with the Department of Communication Engineering,

Northwestern Polytechnical University, Xi'an, where he is currently a Professor. His current research interests include wireless channel measurement and modeling, architecture and protocol design of wireless networks, and satellite communications.

Dr. Zhang was a recipient of the New Century Excellent Talent Grant from the Ministry of Education of China. He has served as a Local Arrangement Co-Chair for the IEEE/CIC International Conference on Communications in China (ICCC), in 2013, and the Industry Track and Workshop Chair for the IEEE International Conference on High Performance Switching and Routing (HPSR), in 2019. He was an Associate Editor of the *Journal of Communications and Networks*.

VOLUME 7, 2019



HAOCHEN XU received the B.S. degree in communication engineering from Northwestern Polytechnical University, Xi'an, China, in 2017, where he is currently pursuing the master's degree with the Department of Communication Engineering. His research interests include wireless channel measurement and modeling, array signal processing, and machine learning in wireless communications.



XIAOJIANG DU received the B.S. and M.S. degrees from Tsinghua University, Beijing, China, in 1996 and 1998, respectively, and the M.S. and Ph.D. degrees from the University of Maryland, College Park, in 2002 and 2003, respectively, all in electrical engineering.

He is currently a Professor with the Department of Computer and Information Sciences, Temple University, PA, USA. His research interests include security, wireless networks, and systems.

He has authored over 250 journals and conference articles in his research areas and a book published by Springer. He has been awarded more than five million U.S. dollars research grants by the U.S. National Science Foundation (NSF), Army Research Office, Air Force, NASA, PA, and Amazon. He won the Best Paper Award from the IEEE GLOBECOM 2014 and the Best Poster Runner-Up Award from ACM MobiHoc 2014. He has served as the Lead Chair for the Communication and Information Security Symposium at the IEEE International Communication Conference (ICC) 2015. He has served as the Co-Chair for Mobile and Wireless Networks Track of the IEEE Wireless Communications and Networking Conference (WCNC) 2015. He is a Life Member of the ACM.



DEYUN ZHOU received the B.S., M.S., and Ph.D. degrees from Northwestern Polytechnical University, in 1985, 1988, and 1991, respectively. His research interests include predictive control, adaptive control, intelligent control theory and its applications, complex system modeling and simulation, multi-objective optimization, information fusion, and complex network modeling and its applications.



MOHSEN GUIZANI (S'85–M'89–SM'99–F'09) received the bachelor's (Hons.) and master's degrees in electrical engineering, and the master's and Ph.D. degrees in computer engineering from Syracuse University, Syracuse, NY, USA, in 1984, 1986, 1987, and 1990, respectively. He is currently a Professor with the Department of Computer Science and Engineering, Qatar University, Qatar. Previously, he has served as the Associate Vice President of graduate studies with Qatar University,

the Chair for the Computer Science Department, Western Michigan University, and the Chair for the Computer Science Department, University of West Florida. He also served in academic positions at the University of Missouri-Kansas City, University of Colorado Boulder, Syracuse University, and Kuwait University. His research interests include wireless communications and mobile computing, computer networks, mobile cloud computing, and security and smart grids. He currently serves on the editorial board of several international technical journals, and the Founder and the Editor-in-Chief of *Wireless Communications and Mobile Computing* journal (Wiley). He is the author of nine books and more than 400 publications in refereed journals and conferences. He was a Guest Editor for a number of special issues in the IEEE journals and magazines. He also served as a member, the Chair, and the General Chair for a number of international conferences. He was selected as the Best Teaching Assistant by Syracuse University for two consecutive years. He received the best research award from three institutions. He was the Chair of the IEEE Communications Society Wireless Technical Committee and the TAOS Technical Committee. He has served as a Distinguished Speaker for the IEEE Computer Society, from 2003 to 2005.

• • •